The contribution of methyl groups to electron spin decoherence of nitroxides in glassy matrices

Samuel M. Jahn,[1] Rachelle K. Stowell,[1] and Stefan Stoll[1]
Department of Chemistry, University of Washington, Seattle, Washington, 98195, USA.

(*Electronic mail: stst@uw.edu)

(Dated: 14 October 2024)

Long electron spin coherence lifetimes are crucial for high sensitivity and resolution in many pulse electron paramagnetic resonance (EPR) experiments aimed at measuring hyperfine and dipolar couplings, as well as in potential quantum sensing applications of molecular spin qubits. In immobilized systems, methyl groups contribute significantly to electron spin decoherence as a result of methyl torsional quantum tunneling. We examine the electron spin decoherence dynamics of the nitroxide radical 2,2,6,6-tetramethylpiperidin-1-oxyl (TEMPO) in both a methyl-free solvent and a methyl-containing solvent at cryogenic temperature. We model nitroxide and solvent methyl effects on decoherence using cluster correlation expansion (CCE) simulations extended to include methyl tunneling and compare the calculations to experimental data. We show that by using the methyl tunneling frequency as a fit parameter, experimental Hahn echo decays can be reproduced fairly well, allowing structural properties to be investigated in silico. In addition, we examine the Hahn echo of a hypothetical system with an unpaired electron and a single methyl to determine the effect of geometric configuration on methyl-driven electron spin decoherence. The simulations show that a methyl group contributes most to electron spin decoherence if it is located between 2.5 and 6-7 Å from the electron spin, with its orientation being of secondary importance.

I. INTRODUCTION

In pulse electron paramagnetic resonance (EPR) spectroscopy experiments, the measured signal is an electron spin echo, formed by rephasing of precessing electron spin magnetic moments within the ensemble of unpaired electrons in the sample. Besides on the length and details of the pulse sequence, the echo amplitude depends on the coherence time of the electron spins. The achievable echo amplitude directly determines the achievable sensitivity and thereby the resolution of many experiments. For a given pulse sequence, shorter coherence times lead to decreased echo amplitudes. Therefore, electron spin (de)coherence is of central practical importance.

Many EPR experiments are performed under cryogenic conditions on immobilized samples of dilute electron spins in matrices that often contain large numbers of magnetic nuclei (e.g. sub-mM electron spins in 110 M protons for water). Under cryogenic conditions, most atoms are to a good approximation fixed in space, so that motional drivers of decoherence are eliminated. Additionally, longitudinal relaxation times are long for organic radicals and low-spin transition metal ions. Electron spin decoherence is then predominantly driven by state mixing between the electron spin and the surrounding nuclear spins, mediated by hyperfine couplings between the electron and the nuclei in combination with dipolar couplings between nuclei. This nuclear-spin-driven electron spin decoherence mechanism has been extensively studied.[1–11] More nuclear spins around the electron tend to reduce the coherence time.[12–16] The decoherence dynamics can be well predicted computationally from a model of the geometric configuration of the electron spin and the surrounding nuclei. These methods use cluster correlation expansion (CCE), one of a group of similar approximate many-body quantum dynamics approaches.[17,18] In previous work, we successfully applied CCE simulations in combination with structural models derived from molecular dynamics to predict and analyze the decoherence dynamics of nitroxides and other radicals in frozen water/glycerol solution in Hahn echo and refocused Hahn echo experiments.[19–21]

An additional mechanism is present in samples that contain methyl groups, such as spin-labelled proteins or spin centers in methyl-containing solvents. Even at cryogenic temperatures, where thermally driven diffusive methyl group rotations are quenched, the low moment of inertia of the methyl group and a comparatively low-barrier rotational potential mean that the three methyl hydrogens are non-negligibly delocalized over three minima. The methyl group can therefore "rotate" via quantum tunneling. This results in measurable effects on electron spin decoherence. For example, examining spin-labelled carbonic anhydrase, Lindgren et al. observed a strong dependence of phase memory times on the location of the spin label, with accelerated decoherence for non-surface locations.[12] Zecevic et al. observed that coherence times of nitroxide radicals in methyl-containing solvents are systematically shorter than in methyl-free solvents.[22] Jackson et al. observed methyl effects on Hahn echo decays of a V(IV) complex in o-terphenyl.[23] Methyl torsional tunneling has been observed spectroscopically via EPR,[24] electron–nuclear double resonance (ENDOR)[25–27] and electron spin echo envelope modulation (ESEEM).[28–31] Important data about methyl rotational potentials has been obtained using inelastic neutron scattering and NMR spectroscopy.[32–34]

Although methyl rotors behave nearly classically at high temperatures, quantum theory is required to accurately describe their behavior at low temperatures. The theory of methyl tunneling ENDOR and ESEEM is well developed, but is focused on individual methyl groups.[25–28] There are only a few reports that shed light on the mechanism how methyls contribute to electron spin decoherence at cryogenic temperatures in systems with many magnetic nuclei. Kveder et al. used CCE to model spin echo decays of a γ-irradiated molec-

ular crystal of 2-methyl-malonic acid with methyl groups effects.[9] Eggeling et al. used a regularization approach to extract information about nitroxide methyl rotational barriers from Hahn echo decays for a nitroxide embedded in a solid matrix of o-terphenyl.[30] More recently, Eggeling et al. explored the effect of methyl tunneling on Hahn echo decays for various alkyl-substituted nitroxides in decalin.[31]

In this paper, we present experiments and simulations that examine the electron spin decoherence behavior of a nitroxide radical, 2,2,6,6,-tetramethylpiperidine-1-oxyl (TEMPO), solvated in a methyl-free and in a methyl-containing solvent. We present an extended CCE approach that is able to include methyl tunneling effects at relatively low orders, with manageable computational cost. In addition, we examine how methyl group position and orientation relative to the electron spin affects electron spin decoherence. We find that the theory can reproduce the experimental Hahn echo reasonably well, and that methyl groups drive electron spin decoherence strongest if positioned between 2.5 and 6-7 Å from the unpaired electron.

II. THEORY

In this section, we summarize the theory for the simulation of the quantum spin dynamics of an isolated electron spin ($S = 1/2$) in a frozen bath of N surrounding nuclear spins (including those on methyl groups) under the influence of a multi-pulse excitation sequence, using a spin Hamiltonian $\hat{H}$. We assume ideal pulses and focus on the Hahn echo sequence, $\pi/2 - \tau - \pi - \tau -$ echo.

A. Spin dynamics and Hamiltonian

In the high-magnetic-field limit, the eigenstates of the electron spin are well described by the quantum number $m_S = \pm 1/2$. With $\langle m_S|\hat{H}|m'_S\rangle \approx 0$ for $m_S \neq m'_S$, the spin Hamiltonian is approximated as block diagonal with two sub-Hamiltonians[35]

$$\hat{H}(m_S = \pm 1/2) := \langle m_S|\hat{H}|m_S\rangle\,. \tag{1}$$

The density operator, $\hat{\rho}$, starts out in thermal equilibrium. A good model at $B_0 = 1.2$ T and $T = 20$ K is that the electron spin is slightly polarized ($\mu_B B_0/k_B T \approx 0.04$), but the nuclei are in the high-temperature limit (since $\mu_N B_0/k_B T \approx 2\times10^{-5}$). This is described by $\hat{\rho} \propto \hat{S}_z$, which is block diagonal with two identity matrices on the diagonal.

To calculate the Hahn echo decay, the density operator is propagated through the pulse sequence with a series of propagators, which are also block diagonal in the chosen high-field approximation.[35] The initial $\pi/2$ pulse converts the initial electron spin polarization into electron spin coherence, mathematically the density matrix subblock $\hat{\rho}^{(-+)} := \langle m_S = -\frac{1}{2}|\hat{\rho}|m_S = +\frac{1}{2}\rangle$ goes from zero to the identity matrix, since the nuclei are in the high-temperature limit.

The two sub-propagators for the free evolution periods are

$$\hat{U}^{(\pm)}(t) = \exp\Big(-\frac{\mathrm{i}}{\hbar}\hat{H}(\pm 1/2)t\Big). \tag{2}$$

The π pulse swaps $\hat{\rho}^{(-+)}$ and $\hat{\rho}^{(+-)}$. With this, the overall propagator for the rest of the pulse sequence is

$$\hat{U}^{(\pm)}_{\mathrm{tot}}(2\tau) = \hat{U}^{(\mp)}(\tau)\hat{U}^{(\pm)}(\tau). \tag{3}$$

The measured signal is proportional to the component of the sample magnetization that is orthogonal to the applied magnetic field. Under quadrature detection, the measured signal is

$$v(2\tau) \propto \mathrm{tr}\Big(\hat{U}^{(-)}_{\mathrm{tot}}(2\tau)\hat{U}^{(+)}_{\mathrm{tot}}(2\tau)^{\dagger}\Big). \tag{4}$$

We use the normalization convention that $v(0) = 1$.

The m_S-dependent spin Hamiltonian is

$$\hat{H}(m_S) = \hat{H}_Z(m_S) + \hat{H}_{\mathrm{hf}}(m_S) + \hat{H}_{\mathrm{dd}} + \hat{H}_{\mathrm{nq}} + \hat{H}_{\mathrm{methyl}}. \tag{5}$$

The Zeeman coupling is modeled as

$$\hat{H}_Z(m_S) = -B_0(-\mu_B g_{zz})m_S - B_0\mu_N\sum_n g_n\hat{I}_{zn}. \tag{6}$$

The applied magnetic field is denoted $\boldsymbol{B}_0$ and $B_0 := |\boldsymbol{B}_0|$. μ_B and μ_N are the Bohr and nuclear magnetons, respectively. With $\hat{\boldsymbol{z}} := \boldsymbol{B}_0/B_0$ as the unit vector along the direction of the applied magnetic field and the electron g-matrix $\boldsymbol{g}$, $g_{zz} := |\hat{\boldsymbol{z}}^{\mathrm{T}}\boldsymbol{g}|$ is the effective g value of the electron. g_n is the nuclear g-factor for nucleus n, and $\hat{I}_{zn}$ is the nuclear z spin operator for nucleus n. The hyperfine coupling is modeled as

$$\hat{H}_{\mathrm{hf}}(m_S) = m_S\sum_{n=1}^{N}\hat{\boldsymbol{z}}^{\mathrm{T}}\boldsymbol{A}_n\hat{\boldsymbol{I}}_n. \tag{7}$$

$\hat{\boldsymbol{I}}_n$ is the vector spin operator for nucleus n. Using the point-dipole approximation, the hyperfine coupling tensor is

$$\boldsymbol{A}_n = \frac{\mu_0}{4\pi}\frac{(-\mu_B g_e)(\mu_N g_n)}{|\boldsymbol{r}_n|^3}\Big(\mathbb{1} - \frac{\boldsymbol{r}_n\boldsymbol{r}_n^{\mathrm{T}}}{|\boldsymbol{r}_n|^2}\Big). \tag{8}$$

where μ_0 is the vacuum permittivity constant, $\mathbb{1}$ is the 3×3 identity matrix, and $\boldsymbol{r}_n$ is the vector from the electron spin to the nuclear spin. For Hahn echo simulations, the point-dipole approximation is good for all nuclei except the TEMPO nitrogen, which is assumed to have $\boldsymbol{A}$ with eigenvalues [20, 20, 100] MHz for ^{14}N and oriented to have its x-axis along the N–O bond and its z-axis normal to the plane defined by the N–O group and the adjacent carbons. The TEMPO hydrogens have some amount of isotropic hyperfine coupling,[36] so it is not clear a priori that the point-dipole approximation for them does not lead to significant errors; to address this, the supplementary material includes Hahn echo simulations where DFT-calculated hyperfine couplings are compared to the point-dipole approximations, leading to the conclusion that the point-dipole approximation works fine for the

Hahn echo simulations of TEMPO in water/glycerol and in *n*-propanol/glycerol.

The nucleus–nucleus dipole–dipole coupling is

$$\hat{H}_{\mathrm{dd}} = \sum_{m=1}^{N-1} \sum_{n=m+1}^{N} \hat{\boldsymbol{I}}_m^{\mathrm{T}} \boldsymbol{b}_{mn} \hat{\boldsymbol{I}}_n \tag{9}$$

with the coupling tensor

$$\boldsymbol{b}_{mn} = \frac{\mu_0}{4\pi} \frac{(\mu_{\mathrm{N}} g_m)(\mu_{\mathrm{N}} g_n)}{|\boldsymbol{R}_{mn}|^3} \left(\mathbb{1} - \frac{\boldsymbol{R}_{mn} \boldsymbol{R}_{mn}^{\mathrm{T}}}{|\boldsymbol{R}_{mn}|^2} \right). \tag{10}$$

Here, $\boldsymbol{R}_{mn}$ is the vector from nucleus m to nucleus n.

Nuclei with $I \geq 1$ have electric quadrupole moments that interact with the local electric-field gradient. For TEMPO in the protiated solvents we will be looking at, TEMPO's ^{14}N is the only nucleus with a quadrupole coupling:

$$\hat{H}_{\mathrm{nq}} = \hat{\boldsymbol{I}}_{^{14}\mathrm{N}}^{\mathrm{T}} \boldsymbol{P} \hat{\boldsymbol{I}}_{^{14}\mathrm{N}}. \tag{11}$$

The quadrupole coupling tensor, $\boldsymbol{P}$, is modeled as having the same eigenvectors as the nitrogen hyperfine coupling tensor, but with eigenvalues of [-1.47, -0.28, 1.75] MHz.[37] The final term in the spin Hamiltonian of Eq. (5), $\hat{H}_{\mathrm{methyl}}$, is discussed in the next section.

B. Methyl torsional tunneling

In this section, we describe how methyl quantum tunneling is included in the spin Hamiltonian. The rotational potential energy function experienced by a methyl group in a non-symmetric environment is typically written as a Fourier series:[34,39]

$$V(\chi) = \tilde{V}_0 + \sum_{k=1}^{\infty} \tilde{V}_{3,k} \cos(3k\chi + \phi_{3k}). \tag{12}$$

The degree of freedom, χ, is an angle that describes the orientation of the methyl group around its symmetry axis (see Fig. 1A). Due to limited experimental resolution, typically only the $k = 1$ term in the sum is observable. Truncating at $k = 1$, defining the barrier height $V_3 := 2|\tilde{V}_{3,1}|$, choosing $\tilde{V}_0$ such that $\min(V) = 0$, and defining $\chi = 0$ at one of the minima yields the simplified rotational potential

$$V(\chi) \approx V_3 \frac{1 - \cos(3\chi)}{2}. \tag{13}$$

This potential function is C_3 symmetric and is illustrated in Fig. 1B. The three-proton permutation group is the symmetric group over three elements, S_3; however, the subgroup Alt(3), the alternating group over three elements is a good approximation.[40,41] Note that Alt(3) is isomorphic to, but conceptually different from the C_3 point group symmetry of the methyl group. Solving the Schrödinger equation for a rigid rotor in the potential of Eq. (13) yields the energy levels shown in Fig. 1C. The rotational ground level is split into one non-degenerate lower and two degenerate higher states. The symmetry labels typically assigned to these states are A, $\mathrm{E_a}$ and $\mathrm{E_b}$,[34,42] where A, $\mathrm{E_a}$, and $\mathrm{E_b}$ are irreducible representations of Alt(3); these labels are those typically assigned to the methyl group and are borrowed from the C_3 point group.

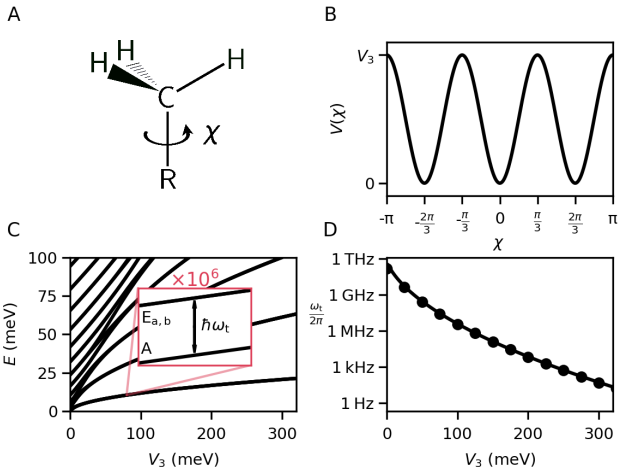

FIG. 1. Structure and energetics of a methyl group. (A) shows a Lewis structure of a methyl group, with the definition of the rotation angle χ. (B) plots the rotational potential energy function against χ. (C) shows how rotational energy levels vary with the barrier height, V_3. While not visible at this scale, the visible energy levels are split into an A state and two degenerate E states, separated by the tunnel splitting for that level. This is shown in the inset at a million times the magnification of the main plot for the ground state at $V_3 \approx 80$ meV, where $\nu_{\mathrm{t}} \approx 18$ MHz. (D) shows the tunnel splitting for the ground librational level, as a function of barrier height. The dots indicate values obtained by numerically diagonalizing the rotational Hamiltonian.[38] The solid line shows the approximate analytic expression of Eq. (14). Note the logarithmic scale of $\omega_{\mathrm{t}}/2\pi$.

The splitting between the A state and the E states is known as the torsional tunnel splitting $h\nu_{\mathrm{t}} = \hbar\omega_{\mathrm{t}}$. The tunnel splitting decreases strongly with increasing V_3; several approximate explicit expressions have been derived,[43–47] one of which is[47]

$$\omega_{\mathrm{t}} \approx 6\sqrt{\frac{3}{\pi}} \left(\frac{2V_3^3}{\hbar^2 I_{\mathrm{methyl}}} \right)^{1/4} \exp\left(-\frac{4\sqrt{2 I_{\mathrm{methyl}} V_3}}{3\hbar} \right). \tag{14}$$

Here, I_{methyl} is the moment of inertia, about $5.3 \cdot 10^{-47}$ kg m^2 = 3.2 u Å^2 for a methyl group with H–H distance of 1.78 Å. The approximation assumes that V_3 is large relative to the rotor's kinetic energy. The $\omega_{\mathrm{t}}(V_3)$ relationship is illustrated in Fig. 1D and compared to numerically exact calculations. The approximation of Eq. (14) overestimates the tunnel splitting by 5% at V_3 = 120 meV and by 10% at 33 meV. Note that as the barrier height increases, the tunnel splitting decreases dramatically. To build some intuition for this, assume the methyl group starts out with a wavefunction localized at $\chi = 0$. This is not a stationary state, and the probability density will spread out with time. There is some characteristic time scale for the methyl group to tunnel through the barriers to give a significant probability density on the other sides of the barriers. This time scale increases with increasing barrier height V_3. As V_3 trends toward infinity, the tunneling time scale goes to infinity,

and the associated frequency goes to zero.

Tunneling frequencies can be inferred from activation energies E_a that can be determined using NMR, via $E_a = V_3 - \hbar\omega_A/2$, where $\hbar\omega_A/2$ is the ground state energy, obtainable by numerically diagonalizing the rotational Hamiltonian for a given V_3. Tunneling frequencies vary over a wide range, as illustrated by the published data on nitroxides and amino acids summarized in Fig. 2.

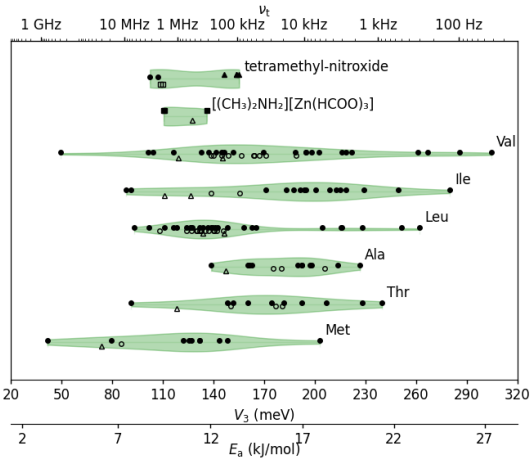

FIG. 2. Published values of experimentally and computationally determined methyl rotation energetics[28–30,48–53] are shown in terms of barrier height V_3, activation energy E_a, and tunnel splitting ν_t. Experimental data are shown as solid shapes, and calculated values are open shapes. Shapes indicate the source of the values. Squares indicate a ν_t source obtained from ESEEM. Triangles indicate a V_3 source from quantum chemical calculations. Circles indicate an E_a source, mostly deuterium NMR for the experimental points and MD for the calculated points.

In order to include methyl quantum tunneling dynamics into spin dynamics simulations, we follow Kveder et al.[9] and use the approach of Apaydin and Clough.[54] In this approach, the rotational Hamiltonian in the rotational ground state (with eight spin-rotational states for a single methyl) is represented as an equivalent exchange spin Hamiltonian (over eight spin states for a single methyl), with one exchange term for each proton pair within the methyl group. This gives the additional Hamiltonian term

$$\hat{H}_{\text{methyl}} = \sum_m \sum_{n>m} J_{mn} \hat{\boldsymbol{I}}_m^{\mathrm{T}} \hat{\boldsymbol{I}}_n. \tag{15}$$

where the sum runs over all unique proton pairs. The exchange coupling, J_{mn}, is defined as

$$J_{mn} := \begin{cases} -\frac{2}{3}\hbar\omega_{t,q}, \text{ if } m \text{ and } n \text{ are on the same methyl } q \\ 0, \text{ otherwise} \end{cases}. \tag{16}$$

For a proton methyl group, this effective Hamiltonian reproduces the splitting of the ground hindered rotational state into a lower-energy ground A state with effective spin 3/2 (four levels) and two degenerate higher-energy E states with effective spin 1/2 (two levels each).

Here, we make the simplifying assumption that ω_t is identical for all TEMPO methyls, and we disregard their potential rotor–rotor coupling.[55] For the propanol solvent methyl groups, we allow for a distribution of ω_t.

C. Cluster Correlation Expansion

In this section, we lay out how the Hahn echo decays are computed, using cluster correlation expansion (CCE).[17,18] CCE is a Hilbert space method for approximately solving the spin quantum dynamics of an individual electron spin in the presence of a large number N of surrounding coupled nuclear spins. For CCE, $v(2\tau)$ in Eq. (4) is Taylor expanded in terms of the nucleus–nucleus couplings, b_{mn}. The resulting series contains an infinite number of terms, each containing operators from a subset of nuclear spins. These subsets are called clusters. The series factors, with one factor per cluster in the resulting product. Sorting the clusters C by the number k of nuclear spins they contain, the full signal is rewritten exactly as

$$v(2\tau) = v^{(N)}(2\tau) := \prod_{k=1}^{N} \prod_{C,|C|=k} \tilde{v}_C(2\tau). \tag{17}$$

where the $\tilde{v}$s are called auxiliary signals and $|C|$ indicates the size of cluster C. This product now has a finite, but very large number of terms. However, it converges rapidly with increasing k as long as the time scale of interest is small relative to all $1/b_{mn}$. In this case, the product over k can be truncated to terms with small cluster size k, and if the maximum cluster size $k_{\max}$ is chosen appropriately, the resulting $v^{(k_{\max})}(2\tau)$ is a reasonable approximation of $v(2\tau)$:

$$v(2\tau) \approx v^{(k_{\max})}(2\tau). \tag{18}$$

We denote this truncated CCE as $k_{\max}$-CCE. $v^{(k_{\max})}(2\tau)$ requires the calculation of $\tilde{v}_C$ for all clusters up to size $k_{\max}$. For clusters of size 1, $\tilde{v}_C$ is equal to the full signal v_C, which is obtained by solving the electron-plus-nucleus system analytically or numerically. For larger cluster sizes, $\tilde{v}_C(2\tau)$ is calculated recursively via

$$\tilde{v}_C(2\tau) = \frac{v_C(2\tau)}{\prod_{C' \subset C} \tilde{v}_{C'}(2\tau)}, \tag{19}$$

where $v_C(2\tau)$ is the exact or full numerical solution for a system consisting of cluster C only, and, under some versions of CCE, the mean-field contribution from the rest of the spins outside the cluster. The division by the product of auxiliary signals of all subclusters of C removes from the exact cluster signal all the terms in the Taylor series that do not contain a spin operator from every spin in the cluster, thus leaving only signal contributions that are due to the presence of all nuclei in the cluster.

For a three-spin system of one electron and two identical spin-1/2 nuclei m and n, if only the secular terms of the hyperfine couplings and the secular and flip-flop terms of the nuclear dipole–dipole coupling are kept, the full signal and

the auxiliary signal for the cluster are identical and have the analytic form[56]

$$\tilde{v}_{\{m,n\}}(2\tau) = v_{\{m,n\}}(2\tau) = 1 - k_{mn}\sin^4(\omega_{mn}\cdot 2\tau). \qquad (20)$$

The parameters in this expression are a modulation depth

$$k_{mn} = \left(\frac{2b_{mn}\Delta A_{mn}}{b_{mn}^2 + \Delta A_{mn}^2}\right)^2 \qquad (21)$$

and an (angular) modulation frequency

$$\omega_{mn} = \frac{1}{8\hbar}\sqrt{b_{mn}^2 + \Delta A_{mn}^2}. \qquad (22)$$

Both depend on the difference of the two secular hyperfine couplings, $\Delta A_{mn} = \hat{\boldsymbol{z}}^{\mathrm{T}}(\boldsymbol{A}_m - \boldsymbol{A}_n)\hat{\boldsymbol{z}}$, and the proton–proton dipole coupling, $b_{mn} = \hat{\boldsymbol{z}}^{\mathrm{T}}\boldsymbol{b}_{mn}\hat{\boldsymbol{z}}$. This represents a modulation of the echo amplitude down from its maximum of 1.[57] For deriving Eq. (20), it is essential to retain the flip–flop term in the Hamiltonian.

For a large system with N nuclei (in addition to the electron), the number of k-clusters is $\binom{N}{k}$. Even for small k, this number is computationally intractable. Therefore, in addition to limiting the maximum cluster size, it is useful to disregard k-clusters with $k \leq k_{\max}$ that are expected to make negligible contributions to the overall signal. The challenge is to identify these clusters without calculating $\tilde{v}_C(2\tau)$ explicitly. Inspired by Jeschke,[57] for $k_{\max} = 2$ we base this additional cluster selection on how much the signals from proton pairs, Eq. (20), deviate from $v_C(2\tau) = 1$. For long 2τ time scales ($2\tau \gg \pi/\omega_{mn}$), the modulation depth, k_{mn}, is a good metric for this. For short 2τ time scales ($2\tau \ll \pi/\omega_{mn}$), the Taylor series expansion of Eq. (20) at $2\tau = 0$ becomes relevant:

$$\tilde{v}_{\{m,n\}}(2\tau) = 1 - k_{mn}\omega_{mn}^4(2\tau)^4 + \mathcal{O}\left((2\tau)^6\right). \qquad (23)$$

The coefficient to the lowest non-constant term, $k_{mn}\omega_{mn}^4$, is a good metric for the deviation of the cluster signal from 1 at short times. Note that $\mathcal{O}\left((2\tau)^6\right) > 0$, so the term containing $k_{mn}\omega_{mn}^4$ overestimates the modulation.

With this, we formulate a combined cluster selection criterion: A particular 2-cluster is included only if both k_{mn} and $k_{mn}\omega_{mn}^4$ are above chosen thresholds, indicating that the cluster contributes on both short and long timescales. For clusters with three or more nuclei, we require the nuclei to form a connected graph with the nuclei as vertices and with an edge defined between a pair of nuclei only if both k_{mn} and $k_{mn}\omega_{mn}^4$ are above threshold. This choice assumes that important k-clusters contain at least $k-1$ important 2-clusters. The supplementary material provides validation tests for this selection criterion.

D. Cluster selection in the presence of methyl groups

The exchange coupling term of Eq. (15) introduced by the finite rotational barrier of methyl groups provides another nucleus–nucleus coupling term. Therefore, the cluster selection criteria must be adjusted when $J_{mn} \neq 0$. For this, we rederive the analytical signal for a three-spin system of one electron and two identical spin-1/2 nuclei, as in Eq. (20), but now in the presence of the additional term $J_{mn}\hat{\boldsymbol{I}}_m^{\mathrm{T}}\hat{\boldsymbol{I}}_n$. Again, only the secular terms of the hyperfine couplings and the secular and flip–flop terms of the nucleus–nucleus dipolar coupling are kept. The exchange coupling term is included in full, as it only contains secular and flip–flop terms:

$$\hat{\boldsymbol{I}}_m^{\mathrm{T}}\hat{\boldsymbol{I}}_n = \hat{I}_{z,m}\hat{I}_{z,n} + \frac{1}{2}\left(\hat{I}_{+,m}\hat{I}_{-,n} + \hat{I}_{-,m}\hat{I}_{+,n}\right). \qquad (24)$$

The result is an expression of the same form as Eq. (20), but with b_{mn} replaced by $b'_{mn} := b_{mn} - 2J_{mn}$. Based on this, we include the tunnel splitting into the cluster selection quantities k_{mn} and $k_{mn}\omega_{mn}^4$ by replacing b_{mn} with b'_{mn} in the expressions for the modulation depth and frequency.

We found that including clusters containing partial methyl groups (only 1 or 2 of a group of 3 methyl protons) occasionally causes simulations to diverge in $k_{\max}$-CCE with $k_{\max} \geq 3$, especially for large tunnel splittings (low barrier heights), i.e. large J_{mn}. Although the precise origin of these divergences remains unclear, it is possible that the large J_{mn} violate the key assumption underlying CCE truncation, i.e. that nucleus–nucleus couplings are small compared to $1/2\tau$. To prevent divergences, clusters that contain partial methyl proton triplets are excluded. This is equivalent to treating the methyls as pseudo-particles: full CCE will still converge to the full solution. What is lost from dropping partial methyls is the ability to distinguish the effects of a single or a pair of protons within a methyl group from the collective effects of the methyl group.

III. COMPARISON WITH EXPERIMENT

To test the methyl-augmented CCE simulation methodology, we examine two experimental systems: dilute solutions of the nitroxide radical TEMPO in 1:1 mass:mass water:glycerol and in 1:3 volume:volume *n*-propanol:glycerol. The first system has methyl groups only on the nitroxide, and the second additionally has methyl groups in the solvent. This choice is based on X-band experiments by Zecevic et al., who measured T_{M} for TEMPONE in these two solvents at 40 K, finding 4.6 µs for water/glycerol and 3.9 µs for *n*-propanol/glycerol.[22]

Samples were prepared by dissolving TEMPO (Sigma–Aldrich) in a 1:1 mass:mass water:glycerol and in 1:3 volume:volume *n*-propanol:glycerol to 200 µM. The EPR experiments were performed at 20 K at Q-band (ca. 33.8 GHz, 1.2 T + δB_0, where δB_0 was selected to maximize the echo amplitude), using dilute nitroxide solutions in quartz tubes (O.D. 1.5 mm, I.D. 1.1 mm; Sutter Instrument). Experiments were performed on a Bruker Elexsys E580 spectrometer equipped with a Bruker D2 dielectric resonator and a 300 W TWT amplifier (Applied Systems Engineering). The pulse sequence used rectangular pulses of 6 ns ($\pi/2$) and 12 ns (π) length. The shot repetition time was 20 ms. Neither longer shot rep-

etition times nor reduced microwave power affected the echo decay shapes.

For the simulations, molecular dynamics (MD) was used to generate structures of the two systems. Using GROMACS 2019.2,[58] a TEMPO molecule was solvated either with 3026 water molecules and 600 glycerol molecules in a box of 56.7 Å edge length, or with 251 *n*-propanol and 775 glycerol molecules in a box with 86.7 Å edge length. The numbers were chosen to target a final box size of 50 Å, but the initial boxes were oversized to easily fit all the molecules. After energy minimization, and a brief NVT and NPT equilibration (100 ps each in 2 fs steps at 300 K), each system was propagated using 1 fs time steps for 85 ns at 300 K with the CHARMM36 force field using the particle mesh Ewald method for long-range electrostatics, the V-rescale modified Berendsen thermostat, and a pressure of 1 bar via the Parrinello-–Rahman barostat. The final box edge lengths were 54.9 Å for water/glycerol and 50.4 Å for *n*-propanol/glycerol. The last 60 ns of the trace were used for the CCE simulations, with 301 frames spaced 0.2 ns apart. Each frame was rotated to a random orientation relative to the external field, the Hahn echo decays for all frames were simulated using CCE, and then averaged over all frames.

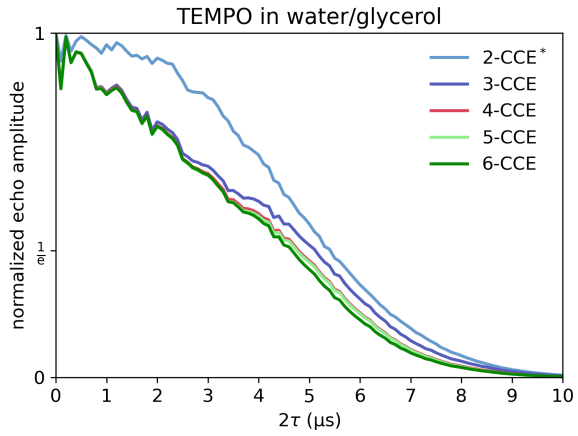

FIG. 3. CCE simulations of the Hahn echo decay of TEMPO in 1:1 mass:mass water:glycerol at a single orientation, using cutoffs of $10^{-7}(\mathrm{rad}/\mu\mathrm{s})^4$ and 323×10^{-7} for $k\omega^4$ and k, respectively, and an 80 kHz tunnel splitting for the TEMPO methyls. (*) Note that since partial methyls are not included, neither methyl tunneling effects nor methyl proton flip-flops are included in 2-CCE.

A. TEMPO in water/glycerol

We first examine TEMPO in water/glycerol. To test convergence with respect to maximum cluster size, we performed truncated CCE simulations using a single MD frame at a fixed orientation. The results are shown in Fig. 3. Since clusters with partial methyl groups are excluded, the 2-CCE simulation does not include any effect of the nitroxide methyl protons. The 3-CCE simulation includes the four methyl groups and is markedly different from the 2-CCE decay. The echo decay is accelerated, and the echo is suppressed particularly at times up to 4 μs. Going to 4-CCE includes clusters with a methyl group and an additional proton, yielding noticeable changes in the later part of the simulated signal. Higher orders do not lead to significant changes, as the 5-CCE and 6-CCE decays are nearly identical to the 4-CCE decays. Therefore, we proceed with 4-CCE. This is in contrast to Kveder et al.,[9] who found that up to 6-CCE can be required in their approach (see discussion below).

Figure 4A shows 4-CCE simulations (colored) using nitroxide methyl tunnel splittings ranging from 0 to 300 kHz in steps of 20 kHz. The calculations show that increasing the tunnel splitting, i.e. lowering the V_3 barrier, leads to shortened coherence times, with significant echo suppression particularly between 0 and 4 μs. The experimental echo decay is shown in black. The TEMPO methyl torsional tunnel splitting that leads to a simulated decay that is closest to the experimental decay (as determined by the RMSD between the simulated trace and the optimally rescaled experimental decay, calculated up to 4 μs; shown in Fig. 4B) is 80 kHz (highlighted with a red dashed line), corresponding to a barrier height of 160 meV (1860 K). This value is close to previous published values (see Fig. 2), with observed nitroxide tunnel splittings ranging

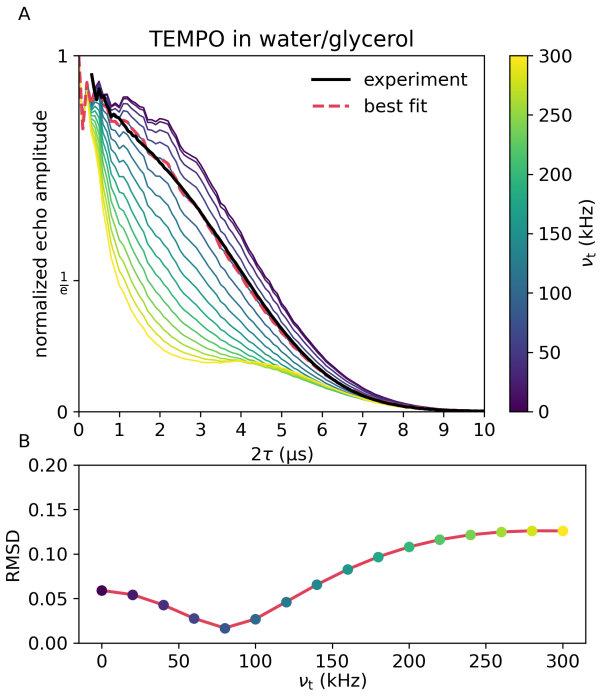

FIG. 4. (A) plots the 20 K experimental (black) and simulated Hahn echo decays of TEMPO in frozen 1:1 mass:mass water:glycerol solution. The color axis indicates the value of the tunnel splitting used for the TEMPO methyls in the simulations. Cutoffs: $10^{-7}(\mathrm{rad}/\mu\mathrm{s})^4$ for $k\omega^4$ and 323×10^{-7} for k. The experimental data is scaled to minimize its RMSD with the 80 kHz tunnel splitting simulation. (B) shows the RMSD of each simulation with the experimental data. In evaluating the RMSD at each tunnel splitting, the scaling of the experimental data was set minimize the RMSD.

from 90 kHz to 2 MHz, and V_3 from 160 meV to 110 meV. The variation in the local environment of the methyls likely explains some of the observed deviation and variation: the literature experiments were in a 2,2,4,4-tetramethylcyclobutan-1,3-dione crystal ($\nu_t = 2$ MHz),[48] a frozen toluene solution (for $\nu_t = 0.6$ MHz),[49] and a o-terphenyl glass (ν_t between 90 and 160 kHz).[30] A possible source of bias in our simulations is that fitting to the Hahn echo will favor the tunnel splittings that contribute significantly on the timescale of the Hahn echo.

B. TEMPO in n-propanol/glycerol

For TEMPO in *n*-propanol/glycerol, there is a large number of solvent methyl groups, so it is worth checking CCE's convergence with maximum cluster size again. Figure 5 shows $k_{\max}$-CCE calculations, for $k_{\max}$ from 2 to 6, for a single frame and orientation from the MD trajectory. The convergence behavior is similar to the one shown in Fig. 3, where only 4 nitroxide methyl groups were present. Here, 3-CCE through 6-CCE are essentially the same. Moving on, we use 4-CCE for several reasons: First, for an odd number o, both o-CCE and $(o+1)$-CCE contribute at the same level[59], so if 3-clusters are included, 4-cluster should be as well; second, 4-CCE is the minimum cluster size that contains clusters including methyl protons and non-methyl protons; third, 4-CCE is what we used in the water/glycerol-solvent case, so 4-CCE allows for a consistent level of approximation.

Kveder et al. found that up to 6-CCE was required to accurately model decoherence in γ-irradiated methyl-malonic acid and acetamide crystals.[9] One possible reason for the difference is that the solvents here have larger proton densities than in the systems investigated by Kveder (110 M for water/glycerol,[60] 113 M for *n*-propanol/glycerol,[61] 77 M for methyl-malonic acid crystal [CSD: MEMALA01], 88 M for acetamide crystal [CSD: ACEMID05]). A higher proton concentration provides more small clusters than a lower proton concentration. There are also more large clusters, but the Taylor series nature of CCE means that small clusters contribute more at short times than large clusters. In addition to spin concentration, time and pulse sequence can make a difference: for higher-order pulse sequences such as Carr-Purcell where electron spin coherence can be maintained longer, higher CCE orders may become necessary.[17] An additional explanation is the difference in cluster selection methodology: Kveder et al. require that the nuclei in a cluster form a complete graph rather than a connected graph, use a nuclear dipole cutoff of 875 s^{-1} for methyl malonic acid and 1125 s^{-1} for acetamide, and place graph edges between all protons on the same methyl group, but do not put any restriction on partial methyl groups within a cluster.[9] If a cluster selection protocol omits some relevant smaller clusters, it might have to compensate for that with the inclusion of larger clusters that contain the omitted smaller cluster. Therefore, the CCE order required for convergence depends not only on sample and experiment, but also on the cluster selection methodology. Simulations must be checked for convergence on a case-by-case basis.

Figure 6A shows the experimental echo decay for TEMPO

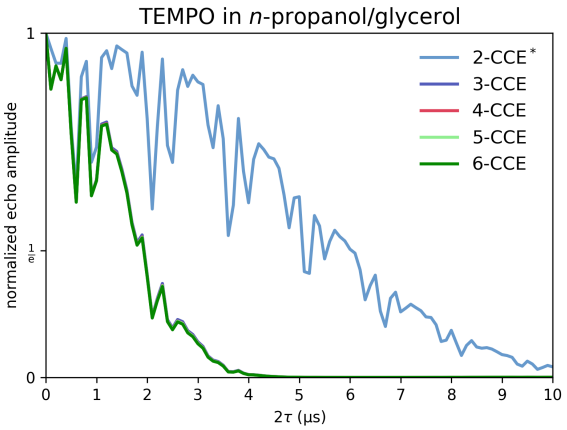

FIG. 5. CCE simulations of the Hahn echo decay of TEMPO in *n*-propanol/glycerol at a single orientation, using cutoffs of $10^{-7}(\text{rad}/\mu\text{s})^4$ and 323×10^{-7} for $k\omega^4$ and k, respectively, and tunnel splittings of 80 kHz kHz for both nitroxide and *n*-propanol methyls. (*) Note that since partial methyls are not included, neither methyl tunneling effects nor methyl proton flip-flops are included in 2-CCE.

in *n*-propanol/glycerol and the associated 4-CCE simulations. The tunnel splitting of the TEMPO methyls was fixed at 80 kHz, as determined from TEMPO in water/glycerol. The tunnel splittings for the *n*-propanol methyls was varied from zero to 1400 kHz. The calculations again show that increasing the tunnel splitting, i.e. lowering the V_3 barrier, leads to shortened coherence times. However, as the tunnel splitting gets large compared with $1/T_M$, the echo amplitude begins to recover. No single tunnel splitting matches the experiment well. For this reason, a linear combination of simulations was selected by non-negative least squares fitting. The fit weights are shown in Fig. 6B. The mode is at 80 kHz, which correspond to a V_3 of 160 meV. In the trans conformer, *n*-propanol has been found to have $V_3 = 118\pm3$ meV using gas-phase microwave spectroscopy.[62] One notable difference between our sample and that of Dreizier[62] is that that our solvent is 1:3 *n*-propanol:glycerol rather than pure *n*-propanol, which might partially explain the difference in V_3 values.

With the best-match methyl tunnel splitting values, we can now analyze individual methyl contributions in more detail. Specifically we use 80 kHz for TEMPO and the 80 kHz mode for *n*-propanol. To aid in this, Fig. 7A shows the electron–methyl radial correlation functions, calculated over all 301 MD frames being used. There is a sharp spike at about 3 Å from the four TEMPO methyls. For *n*-propanol methyls, within about 8 Å, there are more methyl groups than expected from the bulk concentration of 3 M. Using a 2τ resolution of 10 ns, for every methyl, we re-simulated the Hahn echo decay with that particular methyl's tunnel splitting set to zero (i.e. $V_3 \to \infty$). To remove ESEEM modulations, signals were low-pass filtered with a 3rd-order Butterworth filter with a -3 dB frequency of 500 kHz. The filter was applied twice, once forward and once backward. The T_Ms were found by monotonic

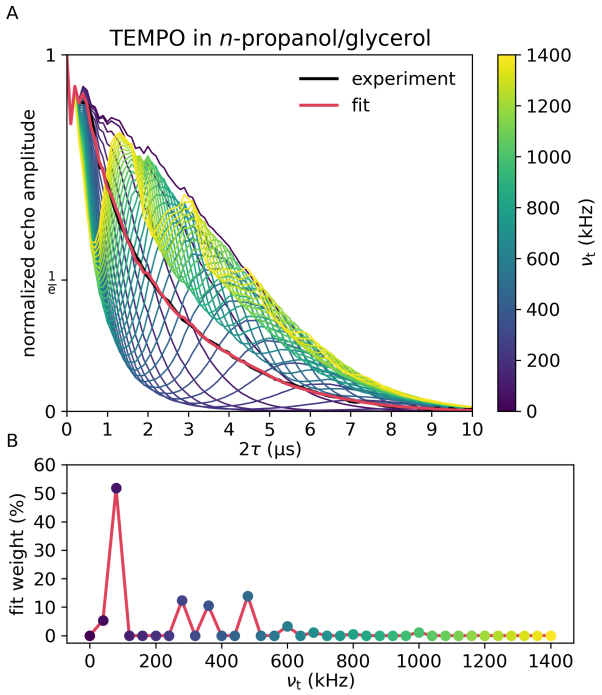

FIG. 6. (A) shows experimental and 4-CCE simulated Hahn echo decays of TEMPO in 1:3 volume:volume *n*-propanol:glycerol solution plotted vs. 2τ. The black trace is the experimental data, acquired at 20 K. The simulations use 80 kHz tunnel splitting for the four TEMPO methyl groups, and varied the *n*-propanol methyl tunnel splitting 0 kHz to 1400 kHz, indicated by the color-axis. Cutoffs: $10^{-7}(\text{rad}/\mu\text{s})^4$ for $k\omega^4$ and 323×10^{-7} for k. The red curve is a linear combination of the simulations from a non-negative least squares fit to the experimental data. The fit and the experimental data are scaled so that the fit is unity at $2\tau = 0$. (B) shows the fit weights against the *n*-propanol methyl tunnel splittings. The fit has RMSD = 0.09, and a coefficient of determination is 0.999. The mode *n*-propanol methyl tunnel splitting is at 80 kHz. The data are colored by their tunnel splitting to make comparisons to the simulated decays easier. Additionally the weights are connected by a red line to guide the eye and show the relationship to the fit in (A).

cubic interpolation of the four closest points to the 1/e time. This allows a methyl tunneling contribution to be defined as the change in T_M when the methyl has a non-zero tunnel splitting compared to when the tunnel splitting is set to zero. The results are shown in Fig. 7B. The TEMPO methyls and the nearest *n*-propanol methyls contribute the most, and then contributions fade with distance from the detected electron. The correlation between methyl contribution and orientation of the methyl group with respect to the electron is much weaker than the distance dependence (see supplementary material). There are few methyl groups where setting the tunnel splitting to zero increases the T_M, meaning that $\Delta T_M < 0$ (these are shown in red in Fig. 7B). The common thread between these methyl groups is that they are all TEMPO methyls and they all have a very small $|\Delta T_M|$, but the exact reason for the ΔT_M sign flip is unclear. The cumulative effect of methyls on T_M is plotted in Fig. 7C. Each line is from one MD frame and represents the T_M obtained from a simulation where the tunnel splittings of all methyls beyond a distance r from the electron spin are set to zero. There is large variation between frames/orientations and so the average over all 301 frames is also shown. The plot shows that nitroxide methyls shorten T_M by about 0.5 μs, and solvent methyl groups within about 7 Å shorten it additionally by 1 μs. Methyl groups beyond that distance from the electron have negligible contribution to the echo decay.

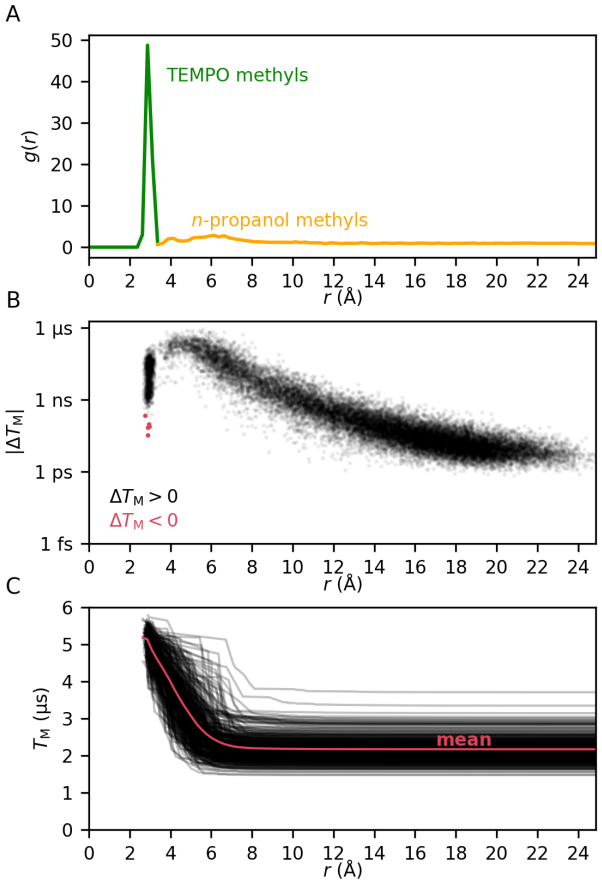

FIG. 7. (A) shows the electron–methyl radial correlation function for TEMPO in *n*-propanol/glycerol over all MD frames. The distances are from the midpoint of the TEMPO NO bond to the centroid of the methyl protons. Color indicates the dominant nature of the methyl groups at each distance, green for TEMPO and yellow for *n*-propanol. (B) plots each methyl from each frame as its distance from the detected electron and the change in T_M when its tunnel splitting is turned off: the black points are for $\Delta T_M > 0$ and indicate that turning the tunnel splitting off lengthens the coherence time, while the red points are for $\Delta T_M < 0$ for the few cases where turning the tunnel splitting off reduces the phase memory time. (C) plots for each of the 301 MD frames the T_M when only methyls up to distance r of the electron have a non-zero tunnel splitting, 80 kHz for both TEMPO and for *n*-propanol. Additionally, the average $T_M(r)$ is shown in red.

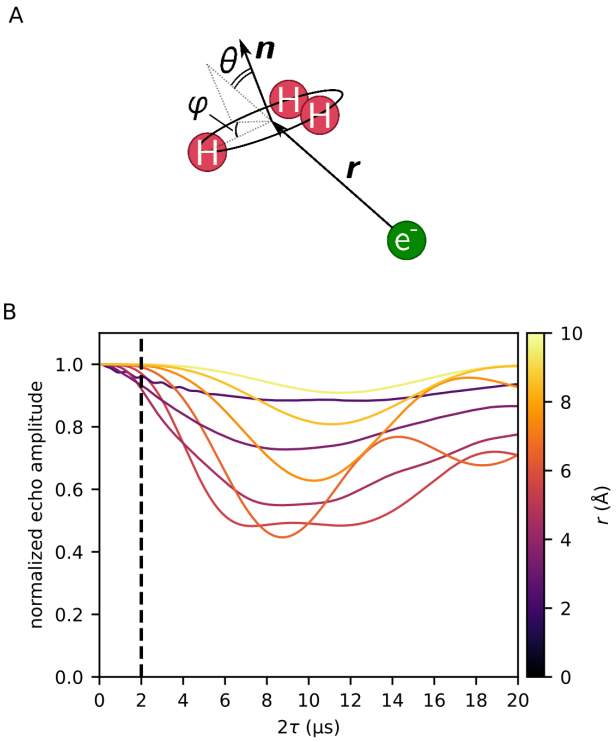

FIG. 8. (A) shows the methyl group at position $\boldsymbol{r}$ relative to the electron; $\boldsymbol{r}$ points toward the methyl proton center of mass. The angle between $\boldsymbol{r}$ and the vector normal to the hydrogen plane, $\boldsymbol{n}$, is denoted θ, and the angle between the projection of $-\boldsymbol{r}$ onto the hydrogen plane and the hydrogen anticlockwise of the projection is ϕ. (B) shows calculated orientationally averaged echo modulations for $\theta = \phi = 0$ and $|\boldsymbol{r}| \in \{2.5, 3.5, 4.5, 5.5, 6.5, 7.5, 8.5, 9.5\}$ Å (indicated on the color axis) and with a 80 kHz methyl torsional tunnel splitting. A dashed line is drawn at $2\tau = 2$ μs.

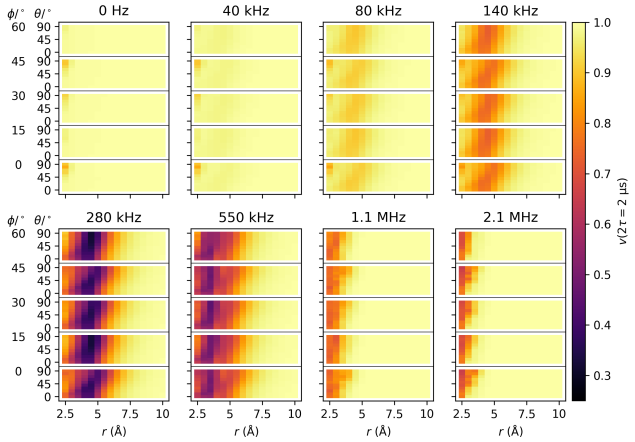

FIG. 9. Echo amplitude $\nu(2\tau = 2\ \mu\text{s})$ vs. $\boldsymbol{r}$ simulated for various tunnel splittings up to 2.1 MHz, are shown as a function of electron–methyl distance (r) and relative methyl orientation (θ and ϕ), using a H–H distance of 1.78 Å and a magnetic field of 1.2 T.

IV. CONTRIBUTIONS FROM AN INDIVIDUAL METHYL GROUP

To further investigate the impact of individual methyl groups on electron spin decoherence, we examine a simple system containing an unpaired electron and the three protons of a single methyl group, as illustrated in Fig. 8A. The internal geometry is characterized by the distance $r = |\boldsymbol{r}|$ between the electron and the center point of the equilateral hydrogen triangle, the H–H distance R_{HH}, the angle θ between $\boldsymbol{r}$ and the triangle normal $\boldsymbol{n}$, and the angle ϕ that describes the in-plane rotation of the hydrogens such that $\phi = 0$ corresponds to one hydrogen lying in the plane defined by $\boldsymbol{n}$ and $\boldsymbol{r}$. Due to the D_{3h} symmetry of the hydrogen triangle, any orientation is equivalent to one with $0 \leq \theta \leq 90°$ and $0 \leq \phi < 60°$. We assume the methyl group has ideal tetrahedral geometry with C–H bond lengths of 1.088 Å,[63] giving a H–H distance of $R_{\text{HH}} = 1.78$ Å. For this small system of four spins, the matrix representations of $\hat{H}(m_S)$ are 8-dimensional, and a full numerical simulation of the spin quantum dynamics is possible.

Figure 8B shows a few exemplary simulated Hahn echo amplitude modulations for $\boldsymbol{n} \| \boldsymbol{r}$ and a range of distances. The echo is orientation averaged over a 1202-point Lebedev grid.[64] Since the system is small, the echo amplitude does not follow a monotonic decay, but rather shows characteristic modulations. It is therefore not possible to define T_{M} here. Instead, we characterize the methyl effect on the echo amplitude by its value at the specific time $2\tau = 2$ μs. This choice is motivated by the fact that for nitroxide radicals in a protiated matrix, 2 μs $\lessapprox T_{\text{M}}/2$, so a methyl group that causes a significant echo loss at 2 μs is expected to make a strong suppression contribution even when solvent proton–proton flip–flops are a strong source of electron spin decoherence.

Figure 9 shows $\nu(2\ \mu\text{s})$ for all possible methyl orientations (θ, ϕ) and a range of distances between 2.5 and 10 Å, in the presence of tunnel splittings up to 2.1 MHz. The plots reveal a strong dependence of the echo suppression on distance and tunnel splitting, but a weaker dependence on the orientation. The suppression is maximal if the tunnel splitting is on the order of hundreds of kHz. The supplementary material shows plots of $\nu(2\tau)$ for other values of 2τ and ν_{t}, which further corroborate this relationship. The figure shows that methyl groups can have a significant echo suppression effect: at ν_{t} of 280 kHz, up to 70% of the echo amplitude can be lost at 2 μs from a single well-placed methyl group. Echo suppression at 2 μs is maximal for distances between 2.5 and 6 Å, although this depends on when the modulation is evaluated. At longer timescale, the upper limit increases to nearly 10 Å at $2\tau = 8$ μs (see supplementary material). This range agrees fairly well with the range found from the simulations for TEMPO in *n*-propanol/glycerol (Fig. 7).

V. CONCLUSIONS

In conclusion, methyl-tunneling-driven electron spin decoherence for TEMPO in proton-rich glassy matrices can be reasonably well modeled with 4-CCE by including the effect of methyl tunneling using the Apaydin–Clough effective spin Hamiltonian and assuming a distribution of tunneling splittings for solvent methyl groups and, separately, uniform tunneling splittings for the four nitroxide methyl groups. The tunnel splitting is sensitive to the local environment. Recently, Eggeling et al. used Hahn echo experiments to infer tunnel splitting distributions of nitroxide methyl groups and found relatively broad distributions of rotation barriers.[30] The modeling accuracy for nitroxide methyl could be potentially further improved by including the effect of methyl–methyl rotor–rotor couplings.[55] Solvent methyl rotation barriers are also dependent on the local environment. For example, the methyl of *n*-propanol is reported to have different tunnel splittings for its trans and gauche rotational isomers.[62]

In general, we find that tunneling methyl groups accelerate electron spin decoherence, particularly if the methyl group is between 2.5 to about 6–7 Å from the detected electron. Compared to the electron–methyl distance, the orientation of the methyl group relative to the electron–methyl direction has less impact.

The mechanism of methyl-tunneling-induced decoherence can be pictured semi-classically as follows: A finite rotational barrier for the methyl group adds an effective nucleus–nucleus spin exchange coupling. This increases the effective nucleus–nucleus flip–flop rate and so too increase the hyperfine-mediated magnetic field fluctuation rate at the position of the detected electron.

Overall, this works provides predictive modeling of and insights into methyl-tunneling-driven electron spin decoherence in disordered systems. This is important for developing potential applications of molecular spin qubits and for studying protein conformations using spin-labeled proteins, which incorporate many methyl-containing amino acids.

CODE

The CCE simulations were done with CluE Oxide, a home-written, open source program. CluE Oxide is available at https://github.com/jahnsam/clue_oxide and at https://crates.io/crates/clue_oxide.

SUPPLEMENTARY MATERIAL

The supplementary material contains details about CCE cluster selection and convergence, the field dependence of decoherence, the effect of isotropic hyperfine couplings, details about calculating individual methyl contributions, and additional lone-methyl simulations.

ACKNOWLEDGMENTS

This work was supported by the National Science Foundation (CHE-2154302, S.S.) and the National Institutes of Health (GM125753 and GM151956, S.S.). Parts of the spectrometer used in this work were funded by the National Institutes of Health (OD021557, S.S.). This work was facilitated through the use of advanced computational, storage, and networking infrastructure provided by the Hyak supercomputer system and funded by the STF at the University of Washington.

REFERENCES

[1] W. B. Mims, K. Nassau, and J. D. McGee, Phys. Rev. **123**, 2059 (1961).
[2] P. L. Stanwix, L. M. Pham, J. R. Maze, D. Le Sage, T. K. Yeung, P. Cappellaro, P. R. Hemmer, A. Yacoby, M. D. Lukin, and R. L. Walsworth, Phys. Rev. B **82**, 201201 (2010).
[3] W.-L. Ma, G. Wolfowicz, N. Zhao, S.-S. Li, J. J. L. Morton, and R.-B. Liu, Nat. Commun. **5**, 4822 (2014).
[4] E. S. Petersen, A. M. Tyryshkin, J. J. L. Morton, E. Abe, S. Tojo, K. M. Itoh, M. L. W. Thewalt, and S. A. Lyon, Physical Review B **93**, 161202 (2015).
[5] S. Lenz, K. Bader, H. Bamberger, and J. Van Slageren, Chem. Commun. **53**, 4477 (2017).
[6] J. Soetbeer, M. Hülsmann, A. Godt, Y. Polyhach, and G. Jeschke, Phys. Chem. Chem. Phys. **20**, 1615 (2018).
[7] J. You, D. Carić, B. Rakvin, Z. Štefanić, K. Užarević, and M. Kveder, J. Chem. Phys. **150**, 164124 (2019).
[8] M. Ye, H. Seo, and G. Galli, npj Comput. Mater. **5**, 44 (2019).
[9] M. Kveder, B. Rakvin, and J. You, J.Chem. Phys. **151**, 3164124 (2019).
[10] J. Soetbeer, M. Millen, K. Zouboulis, M. Hülsmann, A. Godt, Y. Polyhach, and G. Jeschke, Phys. Chem. Chem. Phys. **23**, 5352 (2021).
[11] S. Kanai, F. J. Heremans, G. Wolfowicz, A. C. P., S. E. Sullivan, M. Onizhuk, G. Galli, D. D. Awschalom, and H. Ohno, Proc. Natl. Acad. Sci. USA **119**, e2121808119 (2022).
[12] M. Lindgren, G. R. Eaton, S. S. Eaton, B.-H. Jonsson, P. Hammarström, M. Svensson, and U. Carlsson, J. Chem. Soc., Perkin Trans. 2 , 2549 (1997).
[13] E. Abe, J. Isoya, and K. M. Itoh, Physica B: Condens. Matter **376-377**, 28 (2006).
[14] J. M. Zadrozny, J. Niklas, O. G. Poluektov, and D. E. Freedman, ACS Cent. Sci. **1**, 488 (2015).
[15] M. J. Graham, C.-J. Yu, M. D. Krzyaniak, M. R. Wasielewski, and D. E. Freedman, J. Am. Chem. Soc. **139**, 3196 (2017).
[16] M. J. Graham, M. D. Krzyaniak, M. R. Wasielewski, and D. E. Freedman, Inorg. Chem. **56**, 8106 (2017).
[17] W. Yang and R.-B. Liu, Phys. Rev. B **78**, 085315 (2008).
[18] W. Yang and R.-B. Liu, Phys. Rev. B **79**, 115320 (2009).
[19] E. R. Canarie, S. M. Jahn, and S. Stoll, J. Phys. Chem. Lett. **11**, 3396 (2020).
[20] T. Bahrenberg, S. M. Jahn, A. Feintuch, S. Stoll, and D. Goldfarb, Magn. Reson. **2**, 161 (2021).
[21] S. M. Jahn, E. R. Canarie, and S. Stoll, J. Phys. Chem. Lett. **13**, 5474 (2022).
[22] A. Zecevic, G. R. Eaton, S. S. Eaton, and M. Lindgren, Mol. Phys. **95**, 1255 (1998).
[23] C. E. Jackson, T. Ngendahimana, C.-Y. Lin, G. R. Eaton, S. S. Eaton, and J. M. Zadrozny, J. Phys. Chem. C , acs.jpcc.2c01090 (2022).
[24] T. Yamada, K. Komaguchi, M. Shiotani, N. P. Benetis, and A. R. Sørnes, J. Phys. Chem. A **103**, 4823 (1999).
[25] S. Clough, J. Hill, and F. Poldy, J. Phys. C: Solid State Phys. **5**, 518 (1972).
[26] F. Bonon, M. Brustolon, A. Maniero, and U. Segre, Chemical Physics **161**, 257 (1992).

[27] J. I. Martínez, P. J. Alonso, I. García-Rubio, and M. Medina, Phys. Chem. Chem. Phys. **16**, 26203 (2014).
[28] M. Šimėnas, D. Klose, M. Ptak, K. Aidas, M. Mączka, J. Banys, A. Pöppl, and G. Jeschke, Sci. Adv. **6**, eaba1517 (2020).
[29] G. Usevičius, A. Eggeling, I. Pocius, V. Kalendra, D. Klose, M. Mączka, A. Pöppl, J. Banys, G. Jeschke, and M. Šimėnas, Molecules **28**, 979 (2023).
[30] A. Eggeling, J. Soetbeer, L. Fábregas-Ibáñez, D. Klose, and G. Jeschke, Phys. Chem. Chem. Phys. **25**, 11145 (2023).
[31] A. Eggeling, T. Ngendahimana, G. Jeschke, G. R. Eaton, and S. S. Eaton, Phys. Chem. Chem. Phys. **26**, 15240 (2024).
[32] W. Press, *Single-particle rotations in molecular crystals*, Springer tracts in modern physics No. 92 (Springer Verlag, Berlin Heidelberg New York, 1981).
[33] M. Prager and A. Heidemann, Chem. Rev. **97**, 2933 (1997).
[34] A. Horsewill, Prog. Nucl. Magn. Reson. Spectrosc. **35**, 359 (1999).
[35] S. Stoll and R. D. Britt, Phys. Chem. Chem. Phys. **11**, 6614 (2009).
[36] A. Rockenbauer, M. Györ, H. O. Hankovszky, and K. Hideg, in *Electron Spin Resonance*, edited by M. C. R. Symons (The Royal Society of Chemistry, 1988).
[37] M. de Oliveira, R. Knitsch, M. Sajid, A. Stute, L.-M. Elmer, G. Kehr, G. Erker, C. J. Magon, G. Jeschke, and H. Eckert, PLoS ONE **11**, e0157944 (2016).
[38] R. M. Dimeo, Am. J. Phys. **71**, 885 (2003).
[39] K. W. H. Stevens, J. Phys. C: Solid State Phys. **16**, 5765 (1983).
[40] D. B. Chesnut, *Finite groups and quantum theory*, reprint 1982 (with corrections) ed. (R.E. Krieger Pub. Co, Malabar, Fla, 1982).
[41] P. R. Bunker and P. Jensen, *Molecular symmetry and spectroscopy*, 2nd ed., 46853 (NRC Research Press, Ottawa, 2006).
[42] J. H. Freed, J. Chem. Phys. **43**, 1710 (1965).
[43] M. W. G. Whittall and G. A. Gehring, J. Phys. C: Solid State Phys. **20**, 1619 (1987).
[44] M. W. G. Whittall and G. A. Gehring, J. Phys. A: Math. Gen. **20**, 4035 (1987).
[45] J. Peternelj, I. Jencic, B. Cvikl, and M. M. Pintar, Phys. Rev. B **36**, 25 (1987).
[46] J. Peternelj and I. Jencic, J. Phys. A: Math. Gen. **22**, 1941 (1989).
[47] J. Peternelj, I. Kodeli, and M. M. Pintar, Can. J. Phys. **67**, 1085 (1989).
[48] A. Barbon, M. Brustolon, A. L. Maniero, M. Romanelli, and L.-C. Brunel, Phys. Chem. Chem. Phys **1**, 4015 (1999).
[49] L. V. Kulik, I. A. Grigor'ev, E. S. Salnikov, S. A. Dzuba, and Y. D. Tsvetkov, J. Phys. Chem. A **107**, 3692 (2003).
[50] Y. Xue, M. S. Pavlova, Y. E. Ryabov, B. Reif, and N. R. Skrynnikov, J. Am. Chem. Soc. **129**, 6827 (2007).
[51] Y. E. Shapiro, A. Polimeno, J. H. Freed, and E. Meirovitch, J. Phys. Chem. B **115**, 354 (2011).
[52] L. Vugmeyster, D. Ostrovsky, K. Penland, G. L. Hoatson, and R. L. Vold, J. Phys. Chem. B **117**, 1051 (2013).
[53] F. Hoffmann, F. A. A. Mulder, and L. V. Schäfer, J. Chem. Phys. **152**, 084102 (2020).
[54] F. Apaydin and S. Clough, J. Phys. C: Solid State Phys. **1**, 932 (1968).
[55] G. Jeschke, Appl. Magn. Reson. **53**, 635 (2021).
[56] W. Witzel and S. Das Sarma, Phys. Rev. B **74**, 035322 (2006).
[57] G. Jeschke, J. Magn. Reson. Open **14-15**, 100094 (2023).
[58] M. Abraham, T. Murtola, R. Schulz, S. Páll, J. Smith, B. Hess, and E. Lindahl, SoftwareX **1-2**, 19 (2015).
[59] W. M. Witzel, M. S. Carroll, Ł. Cywiński, and S. Das Sarma, Phys. Rev. B **86**, 035452 (2012).
[60] G. P. Association, *Physical Properties of Glycerine and Its Solutions* (Glycerine Producers' Association: New York, NY, 1963).
[61] Q.-S. Li, M.-G. Su, and S. Wang, J. Chem. Eng. Data **52**, 1141 (2007).
[62] H. Dreizier and F. Scappini, Z. Naturforsch **36**, 1187 (1981).
[63] T. Steiner and W. Saenger, Acta Cryst. **A49**, 379 (1993).
[64] V. Lebedev and D. Laikov, Dokl. Math. **59**, 477 (1999).